PHILOSOPHICAL TRANSACTIONS A

rsta.royalsocietypublishing.org

Research

Article submitted to journal

Subject Areas:
composites, optimisation, robustness

Keywords:
buckling, stiffness tailoring, imperfection sensitivity

Author for correspondence:
R. L. Lincoln
e-mail: reece.lincoln@bristol.ac.uk

THE ROYAL SOCIETY PUBLISHING

Reducing imperfection sensitivity of cylindrical shells through stiffness tailoring and robust optimisation

R. L. Lincoln[1], P. M. Weaver[1], A. Pirrera[1] and R. M. J. Groh[1]

[1]Bristol Composites Institute, University of Bristol, BS8 1TR Bristol, UK

The capabilities of the Rapid Tow Shearing (RTS) process are explored to reduce the well-known imperfection sensitivity of axially-compressed cylindrical shells. RTS deposits curvilinear carbon fibre tapes with a fibre-angle-thickness coupling that enables the in-situ manufacturing of embedded rings and stringers. By blending the material's elastic modulus and wall thickness smoothly across the cylindrical surface, the load paths can be redistributed favourably with a minimal-design approach that contains part count and weight while ameliorating imperfection sensitivity. A genetic algorithm that incorporates realistic manufacturing imperfections and axial stiffness constraints is used to maximise the 99.9% reliability load of straight-fibre (SF) and RTS cylinders. The constraints ensure that reliability does not come at the expense of stiffness. The first-order second-moment method is used to calculate statistical moments that enable an estimate of the 99.9% reliability load. Due to the fibre-angle-thickness coupling of RTS, buckling data are normalised by mass and thickness. Compared to a quasi-isotropic laminate, which corresponds to the optimal eight-layer design for a perfect cylinder, the optimised SF and RTS laminates have a 6% and 8% greater 99.9% normalised reliability load. By relaxing the axial stiffness constraint, the performance benefit can be increased such that SF and RTS cylinders exceed the 99.9% normalised reliability load of an eight-layer quasi-isotropic laminate by 23% and 37%, respectively. Both improvements (constrained and unconstrained) stems largely from a reduction in the variance of the buckling-load distribution, thereby demonstrating the potential of fibre-steered cylinders in reducing the imperfection sensitivity of cylindrical shells.

1. Introduction

Thin-walled cylinders are highly-efficient monocoque shells utilised within the aerospace, civil and energy sectors, amongst others. However, the designers of axially-compressed thin-walled shells must contend with the disparity between theory and experiment as collapse due to the loss of stability often occurs at levels well below the predicted buckling load. Von Kármán and Tsien [1] demonstrated that the post-buckling of a cylinder is dominated by an unstable equilibrium path stemming from a sub-critical bifurcation and, therefore, the cylinder is sensitive to imperfections in the pre-buckling regime. The sensitivity to imperfections was quantified by Koiter [2] in his PhD thesis, whereby small geometric imperfections (of the order of a wall-thickness) were shown to reduce the buckling load dramatically.

The buckling phenomenon can be understood qualitatively from an energy perspective. When a cylinder is compressed, the strain energy of the system increases through the addition of membrane energy. The system is initially stable in this unbuckled state representing a global energy minimum. As the strain energy of the system increases, the energy landscape evolves and a new global minimum, corresponding to a buckled shape, is more energetically favourable. Interestingly, even when the cylinder is still nominally in the pre-buckling state, there exists another disconnected (in axial load *vs* axial compression space) equilibrium state, with just a small energy barrier separating the two regimes. A transition over this so-called mountain-pass point [3] represents the lowest energy pathway that exchanges membrane energy for bending energy and induces buckling. Physically, the mountain pass point materialises as a single dimple on the cylinder surface. Due to the rotational invariance of an isotropic cylinder, the initiation of a single dimple can occur at any circumferential location and is strongly dependent on the precise nature of existing initial imperfections. This phenomenon is described as 'spatial chaos' [4–9] due to its analogy to temporal chaos whereby initial conditions drastically affect loading trajectories through time.

To overcome the aforementioned sensitivity to initial imperfections of axially-compressed isotropic shell, stiffening elements (stringers and rings) are often used. Stiffened, a.k.a. semi-monocoque, shells reduce imperfection sensitivity by breaking the cylinder surface into effective curved panels [10]. This can be explained as follows. Firstly, the reinforcement adds stiffness, which increases the energy required for initiation of lateral deflection and for the loss of stability. Secondly, in addition to retarding the onset of a buckle, stiffeners cause a transition of the critical buckling mode to intra-panel buckling, *i.e.* the panel traps the lateral buckling mode. The latter mode is not only geometrically confined but, more importantly, inherently super-critical and, hence, less sensitive to imperfections. The use of stringers and rings in cylindrical shells is standard practice in thin-walled structural design as, for given load carrying capability, semi-monocoque shells are lighter than their unstiffened counterparts. However, the integration of stiffening elements is resource intensive. Typically, two stages are required to combine the outer skin and the stiffeners, increasing time-to-manufacture and cost, and increasing locations of possible failure (*e.g.* stiffener debonding or cracks in weld lands). Despite these drawbacks, the uncertainty of imperfection-sensitive monocoque cylinders leads designers to choose stiffened shells. However, recent advances in modern composite manufacturing techniques offer the opportunity to design inherently imperfection-insensitive cylinders. These advanced manufacturing techniques create Variable Angle Tow (VAT) composite parts, where fibre paths are curvilinear, in contrast to straight in their straight-fibre (SF) equivalent. By arranging fibre paths in a curved way, the stiffness field, and therefore load path, of an axially-compressed cylinder is not uniform across the surface. This non-uniformity breaks the symmetry of the problem very much like stiffeners do, with similarly positive consequences.

Of all possible VAT technologies, the present work focuses on using Rapid Tow Shearing (RTS)—a derivative of Continuous Tow Shearing with greater deposition rate—developed by Kim *et al.* [11] to overcome the manufacturing defects commonly encountered in Automated Fibre Placement (AFP). AFP, the most common VAT manufacturing technique, developed in the

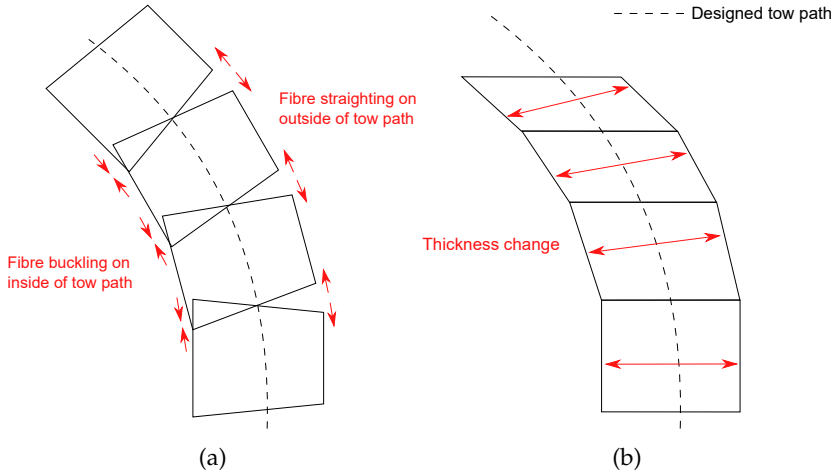

Figure 1: Variable Angle Tow shearing techniques: (a) Automated Fibre Placement (AFP) and (b) Rapid Tow Shearing (RTS). AFP bends the tow along the designed tow path, potentially causing fibre buckling and straightening on the inside and outside of the tow, respectively. RTS shears the tow with respect to the designed tow path, increasing the local thickness and decreasing local width. RTS can tessellate adjacent tows whereas AFP cannot.

1980s [12], places curvilinear fibre paths through in-plane bending of a fibre tow as shown in Figure 1a. As the distance of each fibre in the tow to the central reference path is different, fibre buckling and straightening can occur on the concave and convex side of the tow, respectively [13], as shown in Figure 1a. The mismatch in curvature also eliminates the ability to tessellate adjacent tows, leading to gaps and overlaps that are known to play a significant part in the failure of AFP components [14]. In contrast to AFP, RTS (shown in Figure 1b) shears tows in the plane of placement, creating a uniform radius of curvature across the tape and enabling perfect tessellation of adjacent tows.

In addition to the defect-free manufacturing ability of RTS, it has an interesting geometric feature: fibre-angle-thickness coupling. As a tow is sheared, the local thickness increases perpendicular to the fibre path according to a secant relationship such that the local thickness of the k^{th} RTS lamina in a stack is given by

$$t^k = \frac{t_0^k}{\cos(\theta^k)}, \tag{1.1}$$

where t^k is the local sheared lamina's thickness, t_0^k is the nominal thickness of the unsheared lamina and θ^k is the local lamina shearing angle. The limit to the shearing angle is set by defect-free manufacturing constraints to be 70° [15]. The thickness build-up adds another dimensionality to the design of fibre-reinforced cylinders; embedded stiffeners can now be created by shearing the tow periodically, opening up the possibility to embed hoops, stringers, orthogrids and isogrids within the structure during manufacturing.

Previous numerical [16,17] work has shown that RTS-designed cylinders exhibit reduced sensitivity to geometric imperfections compared to straight-fibre cylinders. To corroborate these results, an RTS and a quasi-isotropic (QI) cylinder were manufactured and tested in axial compression [18]. In the experiment, the RTS cylinder had a 10% greater buckling load than the QI cylinder [18]. Furthermore, finite element (FE) simulations indicate that, if manufacturing imperfections had been equal across both cylinders, the RTS cylinder would have a 10% greater mass-specific buckling load than the QI cylinder. The present work builds on this previous

research by optimising towards an imperfection-insensitive cylinder through robust optimisation and stiffness tailoring.

Optimisation studies of fibre angles for variable-stiffness plates have demonstrated significant weight-savings due to enhanced mechanical properties in pre- and post-buckling [19–21]; reducing stress concentrations around cutouts [22]; and improving buckling of sandwich panels [23]. Variable-stiffness cylinders have been optimised for bending [24,25], buckling [26,27], and fundamental vibration frequency [28] using linear analyses. However, limited work has investigated the optimisation of fibre angle of variable-stiffness cylinders to maximise the nonlinear buckling load in the presence of geometric imperfections. As imperfections are known to reduce the load-carrying capacity of cylindrical shells, an optimisation that accounts for imperfections whilst maximising buckling load could lead to a more imperfection-insensitive design.

For example, Lindgaard *et al.* [29] optimised the fibre angles of a straight-fibre cylinder for nonlinear buckling whilst considering a superposition of eigenmodes as imperfections. The researchers considered this imperfection signature to be the 'worst' as it is "an imperfection shape which yields the lowest limit load" [29]. However, the 'worst' imperfection is known to be the single dimple [3] as it is the lowest energy pathway between pre-buckling and post-buckling regimes. However, both single dimple and eigenmode-affine imperfections are not necessarily realistic imperfections in composite cylinder manufacture, as composite cylinders are typically dominated by low-order periodic modes [30,31].

As imperfections in thin-walled cylinders are stochastic, Bolotin [32] suggested the use of probabilistic analyses to capture the variability of buckling response. A Fourier series representation of measured geometric imperfections is often used as these have been shown to capture the features of realistic imperfection signatures [33]. However, to accurately model a realistic imperfection requires a significant number of Fourier coefficients which can be untenable for a probabilistic methods, such as Monte Carlo analysis. Elishakoff [34] suggested a semi-analytical framework to overcome the computational cost of Monte Carlo analysis referred to as a First-Order Second-Moment (FOSM) method. By using a first-order approximation of the Taylor series expansion of the reliability function to estimate first- and second-moment statistics (mean and variance, respectively), the reliability function can be approximated [35–37]. In this way the computational cost of reliability-based, probabilistic analyses is reduced and can be implemented in an optimisation.

To the authors' knowledge, limited work has been conducted on the optimisation of straight-fibre or tow-sheared composite layups to maximise a conservative buckling estimate of imperfect-geometry cylinders with realistic imperfections, *i.e.* a buckling load in the left tail of the predicted buckling load distribution. The present manuscript addresses this gap within the literature by optimising the fibre angles for maximal 99.9% reliability load of straight-fibre and tow-sheared cylinders with realistic geometric imperfections derived from a data set of measured composite cylinders [35]. Furthermore, a constraint is applied to ensure that the axial stiffness of the cylinder is comparable to a defined baseline cylinder design.

The remainder of paper is structured as follows. Section 2 details the nomenclature and theory of the RTS manufacturing technique. Section 3 describes the FOSM methodology, including estimations of mean and variance, and description of imperfection signatures. Section 4 covers the formulation of the optimisations for the SF and RTS cylinders. Section 5 details the results of the optimisations for the SF and RTS cylinders. Conclusions and areas of future work are summarised in Section 6.

2. RTS nomenclature

To define an RTS lamina, we adapt Gürdal and Olmedo's [38] well-known nomenclature, such that a fibre path is defined by

$$\phi\langle T_0|T_1\rangle^n, \tag{2.1}$$

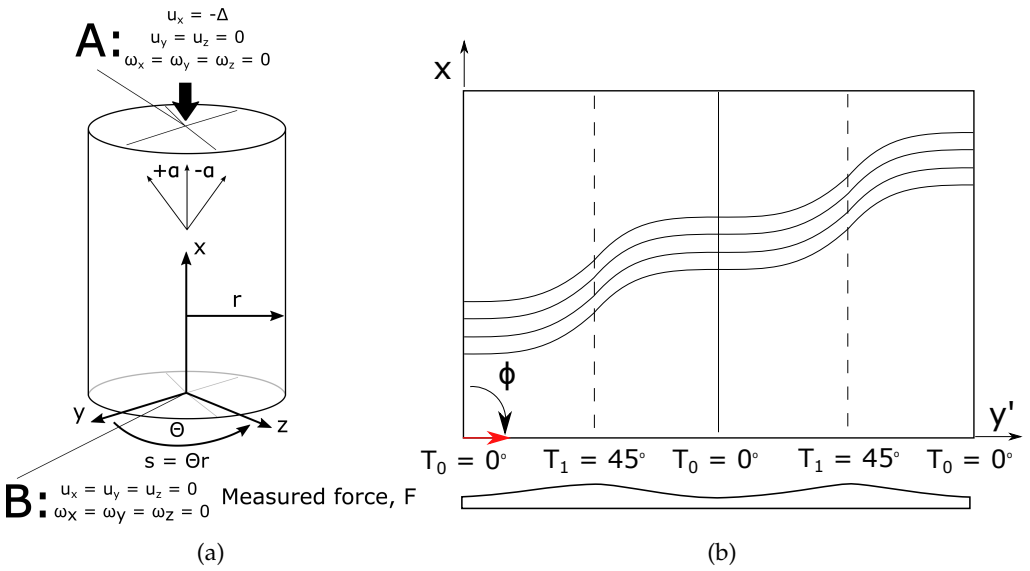

(a) (b)

Figure 2: (a) Coordinate system to define cylinder geometry and boundary conditions used for the FE analyses. Fibre angles are measured counter-clockwise from the global x-axis. Point A corresponds to a multi-point constraint between a reference point at the centroid of the top end of the cylinder and all nodes at the top edge of the cylinder. Five degrees of freedom are constrained at A and only the axial direction, u_x, is free to enforce a displacement, $-\Delta$. Point B is a multi-point constraint between a bottom central reference point and all bottom-edge nodes. All six degrees of freedom are constrained at B. The reaction force of the cylinder is measured at B. (b) A single tow-sheared lamina with the nomenclature as defined in Equation (2.1).

where ϕ defines the direction of the tow-placement head (the steering direction), T_0 defines the initial shearing angle offset from ϕ, T_1 defines the shearing angle in the middle of a shearing period, and n is the shearing periodicity. A $T_0 \rightarrow T_1 \rightarrow T_0$ cycle is one period and it is assumed that the variation in fibre angle between T_0 and T_1 is linear. The direction of the tow-placement head, ϕ, is nominally measured clockwise from the global x-axis (here taken to be the axis of the cylinder), T_0 and T_1 are nominally measured counter-clockwise from the ϕ axis. For SF laminates, fibre angles are measured counter-clockwise from the global x-axis. The coordinate system used herein is shown in Figure 2a.

An application of the nomenclature is shown in Figure 2b for a $90\langle 0|45\rangle^2$ lamina. The cross-section shows that the shearing process creates embedded stiffeners perpendicular to the ϕ direction as a result of the RTS shearing-thickness coupling. In this instance, two embedded stringers are created due the periodicity $n = 2$. By combining $\phi = 0^\circ$ and $\phi = 90^\circ$ plies in a laminate, orthogrid-like structures can be manufactured.

3. First-order second-moment methodology

The following exposition of the FOSM methodology is succinct and the reader is referred to [34,35,37] for further examples and details. The FOSM methodology enables the calculation of statistical moments (mean and variance) by approximating an objective function, $g(\mathbf{x})$—evaluated at a realisation $\mathbf{x}$ of the random vector $\mathbf{X}$ with probability density function $f_{\mathbf{X}}$—by a Taylor series

expanded about the mean vector $\boldsymbol{\mu}$ of $\mathbf{X}$,

$$g(\mathbf{x}) = g(\boldsymbol{\mu}) + \sum_{i=1}^{N} \frac{\partial g(\boldsymbol{\mu})}{\partial x_i}(x_i - \mu_i) + \frac{1}{2}\sum_{i=1}^{N}\sum_{j=1}^{N} \frac{\partial^2 g(\boldsymbol{\mu})}{\partial x_i \partial x_j}(x_i - \mu_i)(x_j - \mu_j) + ..., \tag{3.1}$$

where μ_i is the i^{th} component of the mean vector. In a FOSM analysis, the Taylor series is truncated after the first-order derivative term, such that $g(\mathbf{x}) \approx g(\boldsymbol{\mu})$.

Equation (3.1) describes the Taylor series expansion of $g(\mathbf{x})$, which, we note, is a randomly distributed function, owing to the random distribution of $\mathbf{X}$. For the present analysis, we do not seek an accurate evaluation of the entire distribution of $g(\mathbf{x})$ but rather of points on its tails defining a certain cumulative probability of occurrence. To evaluate specific point of the distribution (say, at a cumulative frequency of 0.01% or 99.9%), approximations of the first and second statistical moments (mean and variance, respectively) can be used. These calculations are discussed in the following subsections.

For Gaussian distributions that are, by definition, fully described by their mean and variance, this method gives exact results. If the distribution is non-Gaussian then the higher-order moments of skewness and kurtosis are generally required to approximate a point within the distribution accurately. Here, by using FOSM, we implicitly make the assumption that the distribution of $g(\mathbf{x})$, *i.e.* the distribution of buckling loads, follows a normal distribution. For subcritical buckling, the distribution of limit loads generally follows extreme value distributions [8,39], but the assumption of normality is often one chosen in the literature for simplicity. In addition, throughout the optimisation process, tow-steered cylinder designs with low variance are automatically chosen as these designs satisfy the objective function of reduced imperfection sensitivity. This leads to the result that Monte Carlo simulations of optimised imperfection-insensitive designs are generally well approximated by a Gaussian distribution.

In conclusion, by means of the FOSM method and based on the assumption of a normally distributed $g(\mathbf{x})$, the 99.9% reliability point, $g^{99.9}$, can be calculated using the relationship between the mean value, μ_g, the standard deviation, σ_g, and a reliability factor, b, such that

$$g^{99.9} = \mu_g - b \cdot \sigma_g, \tag{3.2}$$

The following subsections describe the calculation of the mean (μ_g) and variance (σ_g^2) of $g(\mathbf{x})$.

(a) Mean value of objective function

The mean value of the objective function, μ_g, is found from the expectation operator $\mathbb{E}$ of the objective function

$$\mu_g = \mathbb{E}\left(g(\mathbf{X})\right) = \int_{-\infty}^{\infty} g(\mathbf{x}) f_{\mathbf{X}}(\mathbf{x}) d\mathbf{x}. \tag{3.3}$$

Inserting the truncated first-order approximation of Equation (3.1) into Equation (3.3) leads to the approximation

$$\mu_g \approx \int_{-\infty}^{\infty} \left[g(\boldsymbol{\mu}) + \sum_{i=1}^{N} \frac{\partial g(\boldsymbol{\mu})}{\partial x_i}(x_i - \mu_i) \right] f_{\mathbf{X}}(\mathbf{x}) d\boldsymbol{x} = g(\boldsymbol{\mu}). \tag{3.4}$$

(b) Variance of objective function

The variance, σ_g^2, of $g(\mathbf{x})$ is next calculated. In closed-form, the variance of the objective function is

$$\sigma_g^2 = \mathbb{E}\left([g(\mathbf{X}) - \mu_g]^2\right) = \int_{-\infty}^{\infty} [g(\mathbf{X}) - \mu_g]^2 f_{\mathbf{X}}(\mathbf{x}) d\mathbf{x}, \tag{3.5}$$

which, is equivalent to

$$\sigma_g^2 = \int_{-\infty}^{\infty} g(\mathbf{X})^2 f_{\mathbf{X}}(\mathbf{x}) d\mathbf{x} - \mu_g^2, \tag{3.6}$$

where the mean value of the objective function, μ_g, is calculated from Equation (3.4). When expanded in a first-order Taylor series, the variance is approximated as

$$\sigma_g^2 \approx \int_{-\infty}^{\infty} \left[g(\boldsymbol{\mu}) + \sum_{i=1}^{N} \frac{\partial g(\boldsymbol{\mu})}{\partial x_i} (x_i - \mu_i) \right]^2 f_{\mathbf{X}}(\mathbf{x}) dx - \mu_g^2. \tag{3.7}$$

After simplification, Equation (3.7) reduces to

$$\sigma_g^2 = \sum_{i=1}^{N} \sum_{j=1}^{N} \frac{\partial g(\boldsymbol{\mu})}{\partial x_i} \frac{\partial g(\boldsymbol{\mu})}{\partial x_j} \mathrm{cov}\left(X_i, X_j\right). \tag{3.8}$$

Equation (3.4) together with Equation (3.8) enable the calculation of a high-reliability evaluation of the objective function $g(\mathbf{x})$, as expressed in Equation (3.2). The implementation of the FOSM methodology within an optimisation framework is detailed more fully in Section 4. Before continuing to the optimisation framework it is crucial to consider the variables that comprise the random vector $\mathbf{X}$, *i.e.* the random variables that describe the imperfection signature.

(c) Imperfection signatures

The imperfection signatures used within the optimisations are from a measured set of six composite cylinders [35]. The measured imperfections are decomposed into Fourier coefficients, A_{mn} and B_{mn}, that are used to describe the imperfection field $f(x, s)$ where (x, s) is the cylindrical coordinate system of Figure 2a, with $s = \Theta r$. The axial and circumferential coordinates, x and s, respectively, are scaled to the domain $[-\pi, \pi]$, with a double half-wave cosine function

$$f(x, s) = \sum_{m,n}^{\infty} \lambda_{mn} \Big[A_{mn} \cos(mx) \cos(ns) + B_{mn} \cos(mx) \sin(ns) \Big], \tag{3.9}$$

where A_{mn} and B_{mn} are defined as

$$A_{mn} = \frac{1}{\pi^2} \iint_{-\pi}^{\pi} f(x, s) \cos(mx) \cos(ns) dx ds \,, \tag{3.10}$$

$$B_{mn} = \frac{1}{\pi^2} \iint_{-\pi}^{\pi} f(x, s) \cos(mx) \sin(ns) dx ds, \tag{3.11}$$

with

$$\lambda_{mn} = \begin{cases} 0.25 & \text{for } m = n = 0 \\ 0.5 & \text{for } m > 0, n = 0, \quad \text{or} \quad m = 0, n > 0 \\ 1 & \text{for } m > 0, n > 0 \end{cases}.$$

Two other approaches, double full-wave and double half-wave sine, are methods of approximating the cylinder surface but have ill-defined boundaries. At the boundaries of the double full-wave approach, the surface suffers from the Runge's phenomenon [40,41] whereby high-order functions exhibit spurious oscillations at the edges that are not representative of the imperfection field. When implementing the double half-wave sine approach, the opposite problem occurs—the approximation is unable to capture imperfections at the cylinder top and bottom edges as $\sin \frac{m\pi x}{L} = 0$ for $x = 0$ and $x = L$ where x is the coordinate along the cylinder length.

Equation (3.9) assumes an infinite number of axial (m) and circumferential (n) wave numbers are summed. A limit is typically imposed so that the double half-wave cosine approximation is

$$f(x, s) \approx \sum_{m=0}^{w_1} \sum_{n=0}^{w_2} \lambda_{mn} \Big[A_{mn} \cos(mx) \cos(ns) + B_{mn} \sin(mx) \cos(ns) \Big], \tag{3.12}$$

where w_1 and w_2 are the maximum number of axial and circumferential wave numbers, respectively. Kriegesmann *et al.* [30] suggested using a phase shift approach for cylinders as it

allows for a one-to-one mapping between an imperfection signature and the Fourier coefficients. The new formulation of the half wave cosine phase shift is

$$f(x,s) \approx \sum_{m=0}^{w_1} \sum_{n=0}^{w_2} \lambda_{mn} \left[\zeta_{mn} \cos\left(m\pi \frac{x}{L}\right) \cdot \cos\left(\frac{ny}{r} - \phi_{mn}\right) \right], \tag{3.13}$$

where ζ_{mn} and ϕ_{mn} are described by the relationships

$$\zeta_{mn} = \sqrt{A_{mn}^2 + B_{mn}^2}, \tag{3.14}$$

$$\phi_{mn} = \arctan\left(\frac{B_{mn}}{A_{mn}}\right) \quad \text{for} \quad A_{mn} > 0, \tag{3.15}$$

$$\phi_{mn} = \arctan\left(\frac{B_{mn}}{A_{mn}}\right) + \pi \quad \text{for} \quad A_{mn} < 0, \tag{3.16}$$

$$\phi_{mn} = \operatorname{sgn}\left(B_{mn}\right) \cdot \frac{\pi}{2} \quad \text{for} \quad A_{mn} = 0. \tag{3.17}$$

For the data set considered, w_1 and w_2 are 10 and 20, respectively, representing $N = (10+1)\cdot(20+1)\cdot 2 = 462$ different variables to describe the imperfections of a cylinder. The 462 coefficients are realisations $\mathbf{x}$ of the correlated random variables $\mathbf{X}$ that are used within the FOSM approach such that $\mathbf{x} = [\zeta_{0,0}, \zeta_{0,1}, ..., \zeta_{10,20}, \phi_{0,0}, \phi_{0,1}, ..., \phi_{10,20}]^{\mathrm{T}}$. The implementation of 462 correlated random variables in calculation of derivatives in Equation (3.8) would be computationally expensive as $\mathrm{cov}(X_i, X_j) \in \mathbb{R}^{N\times N}$. To reduce the computational cost, the correlated random variables are transformed into uncorrelated random variables, as discussed in the next subsection.

(d) Data transformation

To simplify the derivatives needed to calculate the mean and variance of the objective function, the vector $\mathbf{X}$ can be transformed with the Mahalanobis transformation [42]. The following description is brief and the reader is directed to References [37] and [35] for further details. The Mahalanobis transformation is defined as

$$\mathbf{X} = \boldsymbol{\Sigma}^{\frac{1}{2}}\mathbf{z} + \boldsymbol{\mu} \quad \text{and} \quad \mathbf{z} = \boldsymbol{\Sigma}^{-\frac{1}{2}}(\mathbf{X} - \boldsymbol{\mu}), \tag{3.18}$$

where the matrix $\boldsymbol{\Sigma}$ is the variance-covariance matrix[‡] of $\mathbf{X}$ and $\mathbf{z}$ is a uncorrelated random vector with mean of 0 and standard deviation of 1. Given a dataset of κ measurements of the uncorrelated random vector $\mathbf{x} \in \mathbb{R}^N$, the variance-covariance matrix $\boldsymbol{\Sigma}$ is estimated by

$$\boldsymbol{\Sigma}(X_i, X_j) \simeq \frac{1}{\kappa - 1} \sum_{k=1}^{\kappa} (\mathbf{x}_i^{(k)} - \boldsymbol{\mu})(\mathbf{x}_j^{(k)} - \boldsymbol{\mu})^{\mathrm{T}}, \tag{3.19}$$

where $\mathbf{x}^{(k)}$ is the k^{th} measurement of the random vector $\mathbf{x}$ and the mean vector, $\boldsymbol{\mu}$, is estimated by

$$\boldsymbol{\mu} \simeq \frac{1}{\kappa} \sum_{i=1}^{\kappa} \mathbf{x}^{(i)}. \tag{3.20}$$

The computed $\boldsymbol{\Sigma}$ and $\boldsymbol{\mu}$ in Equations (3.19) and (3.20) are estimations of the realisations $\mathbf{x}$ in Equations (3.4) and (3.8). As the number of measurements, κ, increases to infinity, the estimations tend to the approximations of Equations (3.4) and (3.8).

Having defined $\boldsymbol{\Sigma}$, it is not generally possible to calculate $\boldsymbol{\Sigma}^{\frac{1}{2}}$ with a Cholesky decomposition, as the matrix $\boldsymbol{\Sigma}$ is usually singular due to the number of measurements, κ, being smaller than the number of random variables, N. In the case considered herein, we have $k = 6$ measured cylinders

[‡]For reference of a matrix to a rational power, the reader is referred to Reference [37]

with a total of $N = 462$ random variables. To overcome this problem, the spectral decomposition of $\boldsymbol{\Sigma}^{\frac{1}{2}}$, defined by $\mathbf{B}$, is determined as

$$\boldsymbol{\Sigma}^{\frac{1}{2}} = \mathbf{B} = \mathbf{Q}\mathbf{D}^{\frac{1}{2}}, \tag{3.21}$$

where $\mathbf{Q} \in \mathbb{R}^{N\times r}$ is a matrix with columns containing the eigenvectors of $\boldsymbol{\Sigma}$, $[\mathbf{q}_1, ..., \mathbf{q}_r]$, and $\mathbf{D} \in \mathbb{R}^{r\times r}$ is a matrix with only diagonal elements containing the eigenvalues of $\boldsymbol{\Sigma}$, $\text{diag}(\sigma_1^2, ..., \sigma_r^2)$. The Mahalanobis transformation is now

$$\mathbf{X} = \mathbf{B}\mathbf{z} + \boldsymbol{\mu} \quad \text{and} \quad \mathbf{z} = \mathbf{B}^{-1}(\mathbf{X} - \boldsymbol{\mu}), \tag{3.22}$$

where the matrix $\mathbf{B} \in \mathbb{R}^{N\times r}$, vector $\mathbf{z} \in \mathbb{R}^r$, and $r = \kappa - 1$ is the number of eigenvectors and eigenvalues of $\mathbf{Q}$ and $\mathbf{D}$, respectively.

Hence, by using the Mahalanobis transformation, the 462 correlated random variables (Fourier coefficients) are decomposed into 5 principal, uncorrelated imperfection modes, greatly reducing the number of partial derivatives computed in the FOSM analysis.

(e) Implementation of transformed data into the reliability equation

The transformation and normalisation of the random vector about its mean is of particular importance when Equation (3.2) is considered with Equations (3.4) and (3.8) substituted so that

$$g^{99.9} \approx g(\boldsymbol{\mu}) - b \cdot \sqrt{\sum_{i=1}^{N}\sum_{j=1}^{N} \frac{\partial g(\boldsymbol{\mu})}{\partial x_i}\frac{\partial g(\boldsymbol{\mu})}{\partial x_j}\text{cov}(X_i, X_j)}, \tag{3.23}$$

where $g(\boldsymbol{\mu})$ is the objective function evaluated at the mean imperfection. Following the Mahalanobis transformation, the vector $\mathbf{X}$ has a variance of 1 and is uncorrelated, simplifying Equation (3.23) to

$$g^{99.9} \approx g(\boldsymbol{\mu}) - b \cdot \sqrt{\sum_{i=1}^{r} \left(\frac{\partial g(\boldsymbol{\mu})}{\partial x_i}\right)^2}. \tag{3.24}$$

The derivative of the objective function with respect to the i^{th} imperfection is evaluated numerically with a central difference scheme

$$\frac{\partial g(\boldsymbol{\mu})}{\partial x_i} = \frac{g(X_{i+\Delta z_i}) - g(X_{i-\Delta z_i})}{2\Delta z_i}, \tag{3.25}$$

where $g(X_{i\pm\Delta z_i})$ is the buckling load of the cylinder with the imperfection signature calculated from the i^{th} imperfection from the transformed dataset where $\Delta z_i = 1.5$ is the finite-difference step size (as calculated from a sensitivity study by Kriegesmann [43]). So, for instance, the calculation of the first imperfection signature with $i = 1$ is

$$\mathbf{X}_{1\pm\Delta z_1} = \begin{bmatrix} B(X_1, X_1) & \dots & B(X_1, X_r) \\ \vdots & \ddots & \vdots \\ B(X_N, X_1) & \dots & B(X_N, X_r) \end{bmatrix} \begin{bmatrix} \pm 1.5 \\ 0 \\ 0 \\ 0 \\ 0 \end{bmatrix} + \begin{pmatrix} \mu_1 \\ \vdots \\ \mu_N \end{pmatrix} \tag{3.26}$$

where the vector $\mathbf{X}_{1\pm\Delta z_1}$ contains the transformed, uncorrelated ζ_{mn} and ϕ_{mn} variables that are used to describe the imperfection signature.

4. Optimisation formulation

Primarily, the objective of the optimisation is to converge on cylinder layups that maximise the buckling load. However, as the RTS process has an angle-to-thickness coupling, as discussed in Section 2, an RTS laminate has a thickness equal to or greater than the unsheared, straight-fibre equivalent. Thus, the mass of an RTS cylinder with shearing will be greater than an SF laminate.

To remove the influence of mass on the buckling load, the mass-specific buckling load can be calculated as $\tilde{P} = P/m$ where P is the buckling load and m is the mass of the cylinder. Nominally, the buckling load of a cylinder [44] given by

$$P = \frac{2\pi r t^2}{\sqrt{3(1-\nu^2)}} \tag{4.1}$$

shows there is quadratic relationship between buckling load and thickness—that is $P \propto t^2$. As $m \propto t$, there is still a first-order relationship between mass-specific buckling load and thickness: $\tilde{P} \propto t$. Therefore the mass-specific buckling load is normalised by thickness so that

$$\hat{P} = \frac{\tilde{P}}{\bar{t}} \tag{4.2}$$

where $\hat{P}$ is the thickness-normalised buckling load and $\bar{t}$ is the average thickness of the laminate. In this way, the RTS laminates and SF laminates can be compared directly as the influence of thickness has been removed.

The layup of the SF cylinder to be optimised is a double angle-ply laminate. Two angles are used in the eight-layer laminate as it enables a comparison to the RTS laminate, a double ply-pair eight-layered laminate. The RTS laminate is a double ply-pair laminate to compare to a previously manufactured RTS cylinder [18]. The SF layup is

$$[\pm\alpha_1, \pm\alpha_2]_\mathrm{s}, \tag{4.3}$$

such that the formulation of the straight-fibre optimisation is

$$\begin{aligned} \max_x \quad & \hat{P}^{99.9}(x) \cdot d(x) \\ \text{Variables} \quad & x = [\alpha_1, \alpha_2] \\ \text{s.t.} \quad & 0 \le \alpha_i \le 90 \ (i = 1, 2) \\ & d(x) = \min\left(1, E_\mathrm{SF}/E_\mathrm{QI}\right)^3, \end{aligned} \tag{4.4}$$

where E_SF and E_QI are the axial stiffness of the SF and QI cylinder, respectively calculated as

$$E = \frac{PL}{2\pi r \bar{t} u}, \tag{4.5}$$

where P is the buckling load, L is the length of the cylinder, r its radius, $\bar{t}$ its average wall thickness and u the applied displacement at the onset of buckling. The 99.9% thickness-normalised buckling load, $\hat{P}^{99.9}$, is calculated from a variation on Equation (**??**) so that

$$\hat{P}^{99.9} = \hat{P}^{\mu} - b \cdot \hat{P}^{\sigma}, \tag{4.6}$$

where b is the chosen reliability limit of 99.9% (which is $b = 3.0902$), $\hat{P}^{\mu}$ is the thickness-normalised buckling load with the mean imperfection signature and $\hat{P}^{\sigma}$ is the standard deviation of the thickness-normalised buckling loads calculated as

$$\hat{P}^{\sigma} = \sqrt{\sum_{i=1}^{r} \left(\frac{\partial \hat{P}^{\mu}}{\partial x_i} \right)^2} \tag{4.7}$$

where $\frac{\partial \hat{P}^{\mu}}{\partial x_i}$ is the i^{th} numerical derivative of the mean thickness-normalised buckling load with the imperfection field $\mathbf{X}_i$ as described in Equation (3.26).

The layup of the RTS cylinder to be optimised is

$$[\phi_1 \pm \langle T_{0_1} | T_{1_1} \rangle^{n_1}, \phi_2 \pm \langle T_{0_2} | T_{1_2} \rangle^{n_2}]_{\mathrm{s}}, \tag{4.8}$$

where ϕ, T_0, T_1, and n have their previous meanings as described in Section 2. The optimisation is formulated for the RTS cylinder as follows

$$\begin{aligned} \max_{x} \quad & \hat{P}^{99.9}(x) \cdot d(x) \\ \text{Variables} \quad & x = [\phi_1, T_{0_1}, T_{1_1}, n_1, \phi_2, T_{0_2}, T_{1_2}, n_2] \\ \text{s.t.} \quad & \phi_i = \{0, 90\} \ (i = 1, 2) \\ & 0 \leq T_{j_i} \leq 70 \ (j = 0, 1, i = 1, 2) \\ & \text{when } \phi_i = 0, \ n_i = 0, 1, 2, ..., 10 \ (i = 1, 2) \\ & \text{when } \phi_i = 90, \ n_i = 0, 1, 2, ..., 18 \ (i = 1, 2) \\ & d(x) = \min \left(1, E_{\mathrm{RTS}}/E_{\mathrm{QI}}\right)^3 \end{aligned} \tag{4.9}$$

where E_{RTS} is the axial stiffness for the RTS cylinder and all other variables have their previous meanings. The fibre angles for the SF and RTS cylinder are always integer values to reflect the accuracy of the RTS method [15].

A genetic algorithm (GA) is used to optimise both straight-fibre and RTS cylinders. The optimisation of fibre angles of composite laminates is known to be a non-convex design problem: results are sensitive to starting points and convergence is not guaranteed [45]. By defining the composite structure with lamination parameters instead of fibre angles the design space can be transformed into a convex design problem under certain conditions [46–49]. A second optimisation step is then required to translate the lamination parameters into a manufacturable layup of fibre angles. For only two unique layers in the laminate stacking sequence (balanced and symmetric layup), the lamination parameter approach is not expected to be faster than an optimisation based on fibre angles directly. Hence, this work conducts the optimisation in fibre angle design space. For verification of the GA, the SF optimised result is compared against an exhaustive search. In addition, the genetic algorithm was verified with benchmark functions to ensure adequate convergence. Both SF and RTS optimisations have a population of 30 and run for 30 generations. For each generation, the number of elite children is 2, the crossover and mutant fractions were 70% and 30% of the remaining population, respectively, reflecting similar values to literature [50].

(a) Geometrically-nonlinear imperfect-geometry buckling analyses

The values of $\hat{P}$ and E are calculated using the commercial FE solver ABAQUS [51]. S4R elements with enhanced hourglassing control are used with the mesh size informed by a convergence study. For a discussion on the discretisation of fibre angles and thicknesses for RTS structures, the reader is directed to [52]. The optimisation is carried out on SF- and RTS-designed cylinders with geometry and material properties as listed in Table 1. For all analyses, wagon-wheel type boundary conditions are used, shown in Figure 2a. The wagon-wheel boundary conditions are implemented with a multi-point constraint between a central control node and the circumferential nodes on the top or bottom of the cylinder. The top reference node is constrained in five degrees of freedom, with the axial direction (x-axis) left free for application of the axial displacement, $u_x = -\Delta$. The bottom reference node is constrained in all six degrees of freedom and the reaction force, F, from the applied displacement, is measured at the reference point. Wagon-wheel type boundary conditions are a standard approach of modelling cylinder buckling in an FE setting [53].

The buckling load of the cylinders with geometric imperfections is calculated using a geometrically nonlinear `Static, General` analysis in ABAQUS. For each analysis the imperfection signatures are implemented in the FE environment through the construction of an orphan mesh based on the number of circumferential and axial nodes. The step size of the

Table 1: Geometry of cylinder and material properties of carbon fibre pre-preg IM7/8552 [54]. The nominal thickness t_0 refers to all eight plies at the unsheared thickness.

r (mm)	L (mm)	t_0 (mm)	E_{11} (MPa)	E_{22} (MPa)	ν_{12} -	G_{12} (MPa)	G_{13} (MPa)	G_{23} (MPa)	ρ (g/mm^3)
300	1040	1.048	138171	9722	0.356	4900	4900	3352	1.57×10^{-3}

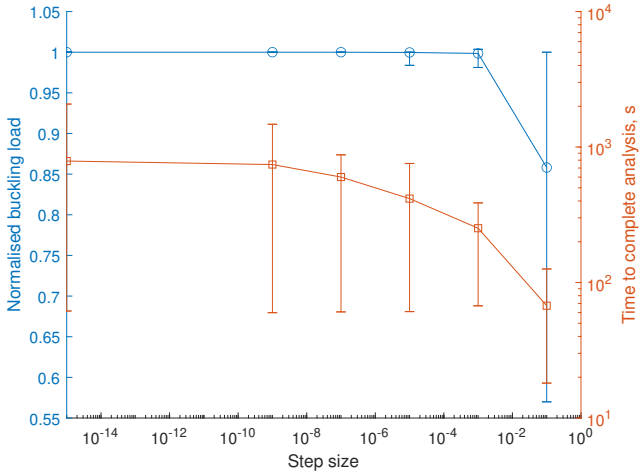

Figure 3: Step size study for 50 random RTS laminates by comparing normalised buckling load and computational time. Normalisation of the buckling load is done with respect to the 1×10^{-15} step size, taken to be most accurate. Data points for load and analysis time represent the arithmetic mean of 50 laminates. Error bars indicate maximum and minimum data points.

incremental-iterative Newton solver is monitored until the solver fails to converge, indicating a limit point instability. The numerical convergence of an imperfect-geometry cylinder is driven primarily by the minimum step size allowed within the Newton solver: the smaller the allowable step size the closer the solver approaches the limit point instability. However, the smaller the allowable step size, the longer the analysis takes. We therefore seek a trade-off between computational accuracy and time. A step-size study is carried out on 50 random RTS laminates to ensure that the selected step size is sufficient to calculate the buckling load accurately whilst balancing computational time.

The results of the step size study are presented in Figure 3, where the normalisation of the buckling load is done with respect to the 'most accurate' results as calculated by the 1×10^{-15} step-size analysis. From Figure 3 it is clear that the step size 1×10^{-3} represents a reasonable trade-off between computational time and accuracy. Thus, this value is used in all further geometrically nonlinear analyses. Quantitatively, the analyses with a step size of 1×10^{-3} have a normalised mean buckling load of 0.999 with a standard deviation of 0.003[†].

In total, 11 geometrically nonlinear analyses are conducted to calculate $\hat{P}^{99.9}$ based on the $\kappa = 6$ imperfection signatures of the measured composite cylinders [35]. The $\kappa = 6$ measured imperfections are decomposed into mean vector ($\boldsymbol{\mu}$) and variance-covariance matrix ($\boldsymbol{\Sigma}$). These data are decomposed into 5 principal imperfection modes using the Mahalanobis transformation and the **B** matrix. Each analysis has a different imperfection signature, created by Equation (3.13). To compute the variance using central finite differences, 10 nonlinear analyses are required

[†]Only 2 of the 50 laminates tested in the 1×10^{-3} step-size analysis were less than 0.995 of the 1×10^{-15} step size analysis.

(forward and backward finite difference steps for each principal imperfection mode). In addition, one analysis is required for the mean imperfection vector. Python [55] scripting is used to pre-process input files, such as defining element-by-element fibre angles, post-process results, and execute the genetic algorithm.

5. Optimisation results

The optimisation was first run on the SF laminate. The $\hat{P}^{99.9}$ values for ply angle combinations are compared to a QI laminate, with a percentage change calculated with respect to the thickness-normalised 99.9% buckling load, $\Delta\hat{P}^{99.9}_{\text{QI}}$, defined as

$$\Delta\hat{P}^{99.9}_{\text{QI}} = 100 \cdot \frac{\hat{P}^{99.9}_{\text{lam}} - \hat{P}^{99.9}_{\text{QI}}}{\hat{P}^{99.9}_{\text{QI}}}, \tag{5.1}$$

where the subscripts lam and QI refer to the laminate considered and QI laminate, respectively.

The QI laminate is chosen as the reference for comparison because it has been shown to be the best straight-fibre laminate for perfect-geometry cylinder buckling [56]. The eight-layer QI, however, is not the overall optimal QI layup due to the deleterious influence of anisotropy [57], as when compared to a homogeneous and specially orthotropic 48-layered QI laminate (*i.e.* no anisotropy) with identical overall thickness, the eight-layer laminate has 89% of the buckling load of the 48-layer one. (The thickness of each ply in the 48-layer QI laminate was scaled to equal the wall thickness of the eight-layer QI.) Nevertheless, given the manufacturing implications of laminating a 48-layer cylinder, the eight-layer QI is taken to be the optimal straight-fibre laminate for perfect cylinder buckling herein. As both an eight-layer QI and eight-layer RTS cylinder have been manufactured and tested [18], we limit the number of plies to be eight to enable comparison between the laminates in this study.

(a) SF results

The solution converged upon by the solver is described in Table 2 as the laminate SF_1 and has a $[\pm 21, \pm 66]_{\text{s}}$ layup. SF_1 has a 5% greater $\hat{P}^{99.9}$ but a 7% lower $\hat{P}^{\mu}$ when compared to the QI laminate, indicating that the greater $\hat{P}^{99.9}$ is due to a reduced standard deviation, $\hat{P}^{\sigma}$. This is indeed the case, with SF_1 having a 54% lower standard deviation than the QI laminate. It appears that in this optimisation, the solver favoured layups with lower standard deviation rather than greater $\hat{P}^{\mu}$. The preference for decreased variance is driven by the high reliability requirement of 99.9% and the $b = 3.0902$ factor used in calculating $\hat{P}^{99.9}$. For example, a decrease in $1\,\text{kN/kg.mm}$ in $\hat{P}^{\sigma}$ increases $\hat{P}^{99.9}$ by $3.1\,\text{kN/kg.mm}$. To explore the design landscape further, and verify the optimisation result, it is informative to perform an exhaustive search of the laminate design space $[\pm\alpha_1, \pm\alpha_2]_{\text{s}}$. We explore the SF design space with an exhaustive search as it is not possible with the RTS laminates due to the high-dimensionality of the RTS layup.

(b) SF exhaustive search

An exhaustive search of the design landscape for the SF layup $[\pm\alpha_1, \pm\alpha_2]_{\text{s}}$ for $\alpha_1, \alpha_2 \in [0, 2, 4, ..., 90]$ is conducted. First, the thickness-normalised linear buckling load, $\hat{P}_{\text{p}}$, of the design landscape is investigated, as shown in Figure 4. The maximal $\hat{P}_{\text{p}}$ is $50.1\,\text{kN/kg.mm}$ in the laminate $[\pm 36, \pm 90]_{\text{s}}$, which is 14.5% lower when compared to the eight-layer QI with a $\hat{P}_{\text{p}} = 58.6\,\text{kN/kg.mm}$. The large valley in the centre of the response surface is attributed to a change in buckling mode shape between a doubly periodic and axisymmetric mode. The response surface has similarities to the unsymmetric laminate $[\pm\beta_1, \pm\beta_2]$ investigated by Hühne [58]. For the material system and geometry of cylinder investigated by Hühne, he found the optimal layup for perfect-geometry buckling load to be $[\pm 20, \pm 35]$. However, for imperfect-geometry buckling, Hühne found the optimal layup to be $[\pm 25, 90_2]$.

Table 2: Data of SF and RTS optimisations. Converged result for RTS and SF optimisations are RTS_1 and SF_1, respectively. SF_2 is the maximum $\hat{P}^{99.9}$ from the exhaustive search for the SF laminate. SF_3 is the maximum fitness value from the exhaustive search for the SF laminate. RTS_2 is the maximum $\hat{P}^{99.9}$ from the RTS optimisation. RTS_{man} is the manufactured cylinder from Ref. [18]. Fit is the fitness value of the layup as calculated from $\text{Fit} = \hat{P}^{99.9} \cdot d(x)$ where $d(x)$ is calculated from the axial stiffness constraint of Equations (4.4) and (4.9). Thickness-normalised results for the 99.9% reliability limit, mean imperfection signature and standard deviation are described by the superscripts 99.9, μ, and σ, respectively. Axial stiffness, E, is calculated from Equation (4.5) and percentage change, $\Delta\hat{P}_{\text{QI}}^{99.9}$, is calculated from Equation (5.1).

ID	Layup	Fit	$\hat{P}^{99.9}$	$\hat{P}^{\mu}$	$\hat{P}^{\sigma}$	E	$\Delta\hat{P}_{\text{QI}}^{99.9}$
			(kN/kg.mm)			(GPa)	(%)
QI	$[\pm 45, 0, 90]_{\text{s}}$	37.7	37.7	47.4	3.13	52.7	-
SF_1	$[\pm 21, \pm 66]_{\text{s}}$	39.6	39.6	44.1	1.45	54.8	5.04
SF_2^*	$[\pm 35, 90_2]_{\text{s}}$	14.7	46.8	50.3	1.16	35.9	23.0
SF_3	$[\pm 22, \pm 66]_{\text{s}}$	40.1	40.1	44.8	1.50	53.2	6.37
RTS_1	$[90 \pm \langle 69 \vert 67 \rangle^{15}, 0 \pm \langle 11 \vert 35 \rangle^{10}]_{\text{s}}$	40.6	40.6	43.1	0.82	53.4	7.69
RTS_2^*	$[90 \pm \langle 58 \vert 67 \rangle^{9}, 0 \pm \langle 64 \vert 64 \rangle^{0}]_{\text{s}}$	27.0	47.7	51.8	1.33	43.6	37.4
RTS_{man}	$[0 \pm \langle 20 \vert 25 \rangle^{2}, 90 \pm \langle 35 \vert 25 \rangle^{9}]_{\text{s}}$	36.3	40.3	46.5	2.01	50.9	6.36

* No axial stiffness constraint

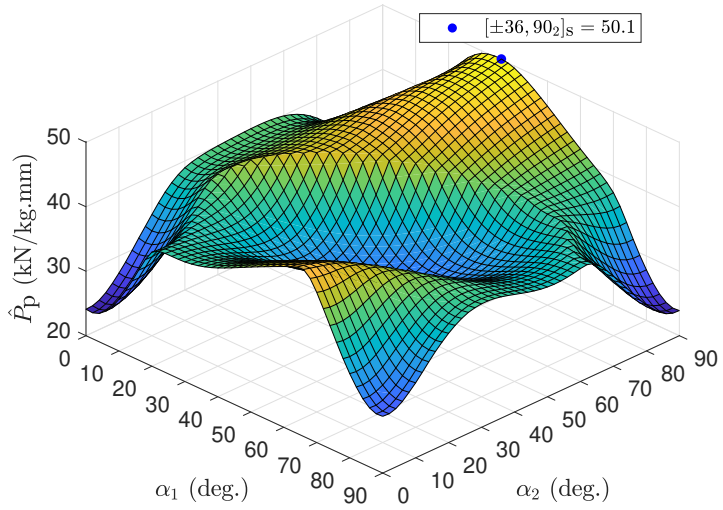

Figure 4: Landscape of the perfect-geometry, thickness-normalised buckling loads $\hat{P}_{\text{p}}$ for $[\pm\alpha_1, \pm\alpha_2]_{\text{s}}$ where $\alpha_1, \alpha_2 \in [0, 2, 4, ..., 90]$. Blue dot is the global maximum $\hat{P}_{\text{p}} = 50.1\,\text{kN/kg.mm}$ for the layup $[\pm 36, 90_2]_{\text{s}}$.

To investigate the imperfect-geometry response of the present structure, a search was conducted with respect to $\hat{P}^{99.9}$ for the $[\pm\alpha_1, \pm\alpha_2]_{\text{s}}$ with $\alpha_1, \alpha_2 \in [0, 5, ...90]$. The design landscape is shown in Figure 5 with the global maximum, SF_2, shown by the red dot and SF_1 shown by the blue dot. The landscape is coarser than Figure 4 as the number of FE analyses to calculate a central difference $\hat{P}^{99.9}$ for 2° increment across $[\pm\alpha_1, \pm\alpha_2]_{\text{s}}$ is 23276 compared to 3971 for a 5° increment. An initial coarse-mesh analysis sweep of the landscape enabled a finer

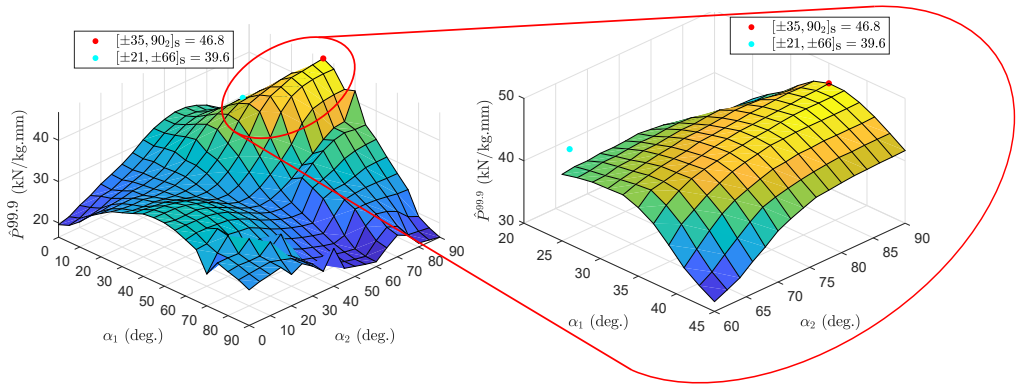

Figure 5: Coarse and fine mesh design landscape of the 99.9% reliability thickness-normalised buckling loads, $\hat{P}^{99.9}$, for $[\pm\alpha_1, \pm\alpha_2]_s$ where $\alpha_1, \alpha_2 \in [0, 5, ..., 90]$. Red dot is the global maximum $\hat{P}^{99.9} = 46.8$ kN/kg.mm for the layup $[\pm35, 90_2]_s$. Cyan dot is optimiser solution SF_1 with $\hat{P}^{99.9} = 39.6$ kN/kg.mm for the layup $[\pm21, \pm66]_s$. Cyan and red dots refer to axial stiffness constraint and no axial stiffness constraint solutions, respectively.

mesh analysis around the global optimum. The global maximum $\hat{P}^{99.9}$ is a $[\pm35, 90_2]_s$ laminate with a $\hat{P}^{99.9} = 46.8$ kN/kg.mm, 23% greater than the QI laminate and 18.2% greater than SF_1. The optimiser did not find laminate SF_2 as it does not meet the axial stiffness constraint and is therefore penalised during the optimisation. As shown in Table 2, the fitness value of SF_2 is 14.7 kN/kg.mm due to the lower axial stiffness of the design and the heavy penalisation due the constraint $d(x)$.

The fitness response surface is depicted in Figure 6 for both a coarse initial mesh and finer mesh in the region of interest. The large valley shown for $\alpha_1, \alpha_2 \geq 35^\circ$ is due to the axial stiffness constraint reducing the fitness of the design. The loss in axial stiffness occurs as the fibres are orientated circumferentially rather than axially. In the analysis of the fitness function, two optima were found based on the coarseness of the fibre angle distribution for the $[\pm\alpha_1, \pm\alpha_2]_s$ layup. The first optimum found in the coarse mesh, a $[\pm20, \pm65]_s$ layup, has a fitness value of 39.1 kN/kg.mm. The second optimum found in the finer mesh, SF_3, a $[\pm22, \pm66]_s$ layup, has a fitness value of 40.1 kN/kg.mm. For layups that have an axial stiffness equal to or greater than the QI, the fitness values are equal to the $\hat{P}^{99.9}$ of that laminate. The $\hat{P}^{99.9}$ of SF_3 is 1.3% greater than the $\hat{P}^{99.9}$ of SF_1, the design found by the optimiser, indicating that the optimisation algorithm converged close to the optimal design. Whilst the convergence of the SF optimisation does not guarantee convergence for the RTS optimisation, it indicates that the optimiser successfully converges *towards* high-reliability, thickness-normalised buckling loads. With the SF design landscape explored and optimisation scheme verified, the RTS results are discussed next.

(c) RTS results

The solution converged upon by the RTS solver, RTS_1, is a $[90 \pm \langle 69|67\rangle^{15}, 0 \pm \langle 11|35\rangle^{10}]_s$ laminate with a $\hat{P}^{99.9} = 40.6$ kN/kg.mm, 7.69% greater than the eight-layer QI laminate and 1.2% greater than SF_3. The optimiser has again converged on a laminate that minimises variance with $\hat{P}^{\sigma} = 0.82$ kN/kg.mm for RTS_1 being 73% lower than the eight-layer QI laminate and 43% lower than SF_1. The orthogrid-type structure produced by RTS_1 is similar to other RTS laminates that have high buckling loads [16] and the manufactured and tested RTS laminate, RTS_{man} [18]. The inner plies have shallow shearing angles, create embedded hoops and have an average thickness of 8% greater than the nominal ply thickness. It is interesting to note the high shearing angles of the first ply-pair of RTS_1—the average thickness of the outer plies is 164% greater than the

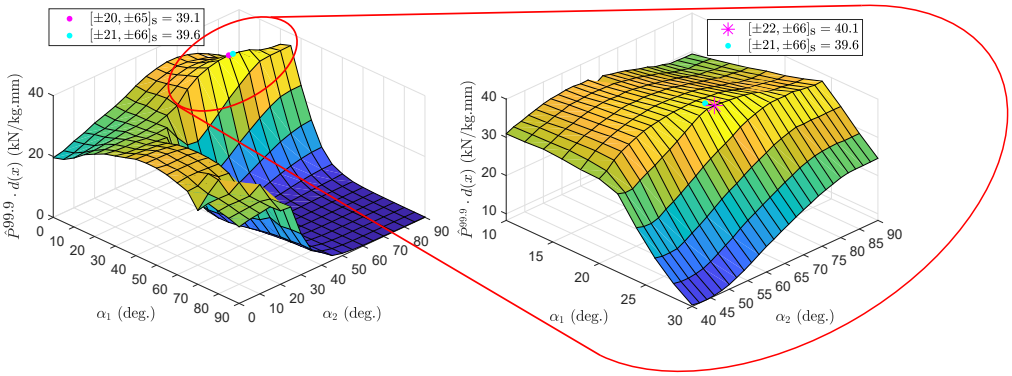

Figure 6: Coarse and fine mesh design landscape of the fitness (Fit) values $\text{Fit} = \hat{P}^{99.9} \cdot d(x)$ for $[\pm\alpha_1, \pm\alpha_2]_s$ where $\alpha_1, \alpha_2 \in [0, 5, ..., 90]$ and $d(x)$ is the axial stiffness constraint described in Equations (4.4) and (4.9). Magenta dot and star represent the global maximum Fit for the coarse and fine mesh respectively. Maximum course mesh $\text{Fit} = 39.1\,\text{kN/kg.mm}$ with layup $[\pm 20, \pm 65]_s$. Maximum fine mesh $\text{Fit} = 40.1\,\text{kN/kg.mm}$ with layup $[\pm 22, \pm 66]_s$. Cyan dot is optimiser solution SF_1 with $\text{Fit} = 39.6\,\text{kN/kg.mm}$ for the layup $[\pm 21, \pm 66]_s$.

nominal thickness. However, despite the increase in average thickness, the thickness-normalised reliability buckling load is still greater than the QI laminate and SF laminates within the axially-constrained optimisation. As the difference between T_0 and T_1 is small, it appears that the optimiser has resulted in a uniformly thick outer ply-pair to increase its contribution to the second moment of area.

It is worth noting that some laminates within the optimisation have greater $\hat{P}^{99.9}$ then the optimised results, but are penalised due to the axial stiffness constraint. The RTS cylinder with the greatest $\hat{P}^{99.9}$, RTS_2 with layup $[90 \pm \langle 58|67\rangle^9, 0 \pm \langle 64|64\rangle^0]_s$, has $\hat{P}^{99.9} = 47.7\,\text{kN/kg.mm}$, which is 37.4% greater than the eight-layer QI cylinder. The $\langle 64|64\rangle^0$ lamina is a sheared, straight-fibre layer that has a thickness 128% greater than the nominal thickness. RTS_2 has a lower fitness value than RTS_1, as the axial stiffness is 17% lower than the eight-layer QI cylinder. However, it worth mentioning that for the SF and RTS cylinders without axial stiffness constraint, *i.e.* SF_2 and RTS_2, the RTS design achieves a better compromise between increased 99.9% reliability load and axial stiffness. While RTS_2 improves on the QI 99.9% reliability load by 37.4% it only has a 17.3% reduction in axial stiffness, whereas SF_2 loses 31.9% of its axial stiffness compared to the QI laminate for a 23.0% improvement in 9.9% reliability load. Hence, the greater design space of tow steering provides the RTS design greater flexibility to obtain high imperfect buckling loads with stiff axial response.

The manufactured RTS cylinder, RTS_{man} has similar $\hat{P}^{99.9}$ and E values to the optimiser-found solution, RTS_1. RTS_{man} was a laminate design with a high fitness value in a dynamic-imperfection optimisation [17] based on a random combination of the first twenty eigenmodes of the QI cylinder. In each generation, the weighting of eigenmodes was changed to 'dynamically' vary the imperfection and incorporate a first-order robustness analysis. The optimisation function maximised the imperfect-geometry buckling load of the RTS laminates with the eigenmode-affine imperfection signature. Despite the higher-order QI eigenmodes not being representative of composite cylinders, which are actually dominated by low-order modes [35], the dynamic optimisation converged on a relatively robust layup that has a high $\hat{P}^{99.9}$, albeit with a slightly lower E as this was set to 90% of the QI stiffness during this optimisation.

To investigate the trade-off between $\hat{P}^{99.9}$ and E further, RTS and SF data from both optimisations are plotted on a single plot, as shown in Figure 7. The green lines represent the QI data for $\hat{P}^{99.9}$ (y-axis) and E (x-axis), respectively. Of the laminates analysed, there are many layups that have greater $\hat{P}^{99.9}$ than the eight-layer QI cylinder, but have lower axial stiffness.

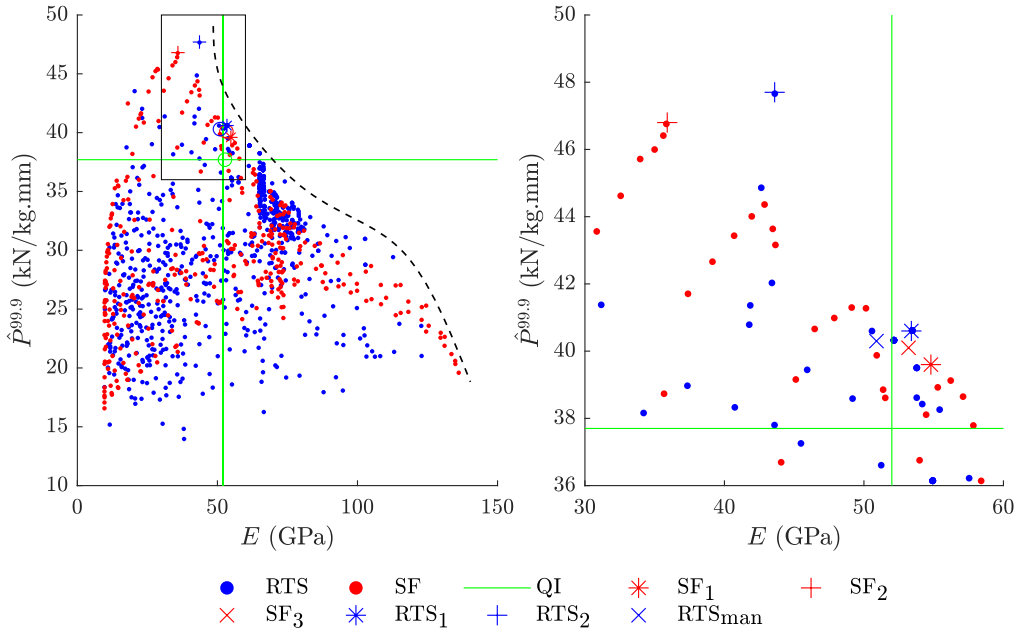

Figure 7: Data from RTS (blue) and SF (red) optimisations. QI data are shown as green lines for $\hat{P}^{99.9}$ (y-axis) and E (x-axis), respectively. Layups tabulated in Table 2 are plotted with different markers. Note the optimisation analyses found solutions that have $\hat{P}^{99.9}$ and E greater than the eight-layer QI. Boxed region is shown on the right-hand side as zoomed-in figure.

Many SF and RTS laminates have a greater E than the QI cylinder, but often to the detriment of $\hat{P}^{99.9}$. Only 13 of the 1261 layups investigated have a greater $\hat{P}^{99.9}$ and E than the eight-layer QI cylinder, indicating that a trade-off is necessary to achieve one over the other. Indeed, the results suggest a Pareto front generated by the data, as shown by the dotted black line in Figure 7, which indicate possible optimal combinations of $\hat{P}^{99.9}$ and E.

6. Conclusion

On account of the susceptibility of thin-walled cylinders to buckle prematurely due to initial imperfections, VAT composites have been investigated as a potential avenue for alleviating imperfection sensitivity. Whilst previous research has optimised the layup of variable-stiffness cylinders for perfect-geometry buckling, the present research offers a novel methodology by including realistic imperfections within the optimisation and optimising the fibre angles for imperfect-geometry buckling load. The imperfections included in the optimisation are taken from a measured data set and are therefore realistic manufacturing imperfections. To offer a statistically significant estimation of robustness, the first-order second-moment methodology of estimating the probability distribution of buckling loads as a function of this measured data set was implemented within the optimisation. Using the Mahalanobis transformation and spectral decomposition, it was possible to reduce the number of analyses needed considerably to calculate statistical features of the estimated distribution. The 99.9% reliability point on the estimated reliability curve was optimised, as it represents a realistic lower-bound for cylinder design (1 in 1000 failure rate). Due to the fibre-angle-thickness coupling of RTS laminates the 99.9% buckling load was normalised by mass and thickness to allow for a fair comparison with constant-thickness designs. Furthermore, an axial stiffness constraint was included within the optimisation to ensure that the optimised buckling load of a design is not to the detriment of other mechanical properties.

Both SF and RTS cylinders were optimised to maximise $\hat{P}^{99.9}$ and compared against an eight-layer QI cylinder. For the straight-fibre optimisation, the optimiser converged on SF_1, a $[\pm 21, \pm 66]_s$ layup that has a 5% greater $\hat{P}^{99.9}$ than the nominal eight-layer QI laminate. An exhaustive search across the $[\pm\alpha_1, \pm\alpha_2]_s$ landscape found that the optimum $\hat{P}^{99.9}$ with axial stiffness constraint is a $[\pm 22, \pm 66]_s$ laminate that has a 6% greater $\hat{P}^{99.9}$ than the QI laminate. Without an axial stiffness constraint, the SF laminate with the greatest $\hat{P}^{99.9}$ is a $[\pm 35, \pm 90]_s$ layup that has a 23% greater $\hat{P}^{99.9}$ but a 32% lower E than the QI laminate. For the RTS laminates, the optimiser converged on RTS_1, a $[90 \pm \langle 69|67\rangle^{15}, 0 \pm \langle 11|35\rangle^{10}]_s$ layup that has a 8% greater $\hat{P}^{99.9}$ than the eight-layer QI cylinder. Another laminate, RTS_2 with layup $[90 \pm \langle 58|67\rangle^{9}, 0 \pm \langle 64|64\rangle^{0}]_s$, has a 37% greater $\hat{P}^{99.9}$ but 17% lower E than the QI laminate.

Despite the convergence on high-reliability laminates, some limitations of the present work offer interesting avenues for further research. To address the time and computational cost of numerous analyses, it is suggested that surrogate modelling [59] would be an efficient methodology to pursue. Presently, the 99.9% reliability point has been used in the objective function with the assumption of normally distributed imperfect buckling loads. Further research into other reliability points (95%, 99%) could be of interest for less safety-critical structures and, if appropriate, assuming different distributions. For example, extreme value distributions generally govern the statistics of subcritical buckling phenomena [8]. Finally, the highly-reliable SF and RTS laminates optimised herein present promising layups that could be manufactured to verify their performance.

Data Accessibility. Data are available at the University of Bristol data repository, data.bris, at https://data-bris.acrc.bris.ac.uk

Authors' Contributions. R.L.L. performed the data analysis in consultation with P.M.W., A.P., and R.M.J.G. R.L.L. drafted the manuscript with input from P.M.W., A.P., and R.M.J.G. All authors read and approved the manuscript.

Competing Interests. The authors declare that they have no competing interests.

Funding. R.L.L. acknowledges the support of the EPSRC [Grant No. EP/L016028/1]. P.M.W. acknowledges the support of the Royal Society Wolfson Merit award and the Science Foundation Ireland for the award of a Research Professor grant [Varicomp: 15/RP/2773]. R.M.J.G. acknowledges the support of the Royal Academy of Engineering under the Research Fellowship scheme [Grant No. RF/201718/17178].

Acknowledgements. This work was carried out using the computational facilities of the Advanced Computing Research Centre, University of Bristol - http://www.bristol.ac.uk/acrc/.

References

1. T. von Kármán and H.-S. Tsien, "Buckling of thin cylindrical shells under axial compression," *Journal of the Aeronautical Sciences*, vol. 8, no. 8, pp. 303–312, 1941.
2. W. T. Koiter, "A translation of: The Stability of Elastic Equilibrium," tech. rep., NASA TT-F-10833, 1967.
3. J. Horák, G. J. Lord, and M. A. Peletier, "Cylinder Buckling: The Mountain Pass as an Organizing Center," *Society for Industrial and Applied Mathematics*, vol. 66, no. 5, pp. 1793–1824, 2006.
4. J. M. Thompson and L. N. Virgin, "Spatial chaos and localization phenomena in nonlinear elasticity," *Physics Letters A*, vol. 126, no. 8-9, pp. 491–496, 1988.
5. G. W. Hunt and M. K. Wadee, "Comparative lagrangian formulations for localized buckling," *Proceedings of the Royal Society of London. Series A: Mathematical and Physical Sciences*, vol. 434, no. 1892, pp. 485–502, 1991.
6. G. W. Hunt, R. Lawther, and P. P. E. Costa, "Finite element modelling of spatially chaotic structures," *International Journal for Numerical Methods in Engineering*, vol. 40, no. 12, pp. 2237–2256, 1997.
7. R. M. J. Groh and A. Pirrera, "On the role of localizations in buckling of axially compressed cylinders," *Proceedings of the Royal Society A: Mathematical, Physical and Engineering Sciences*,

vol. 475, no. 2224, 2019.
8. R. M. J. Groh and A. Pirrera, "Spatial chaos as a governing factor for imperfection sensitivity in shell buckling," *Physical Review E*, vol. 100, no. 3, pp. 1–6, 2019.
9. R. M. J. Groh, G. W. Hunt, and A. Pirrera, "Snaking and laddering in axially compressed cylinders," *International Journal of Mechanical Sciences*, vol. 196, no. December 2020, 2021.
10. M. C. Niu, *Airframe Structural Design*.
Hong Kong: Hong Kong Conmilit Press Ltd., 2nd ed., 1988.
11. B. C. Kim, K. Potter, and P. M. Weaver, "Continuous tow shearing for manufacturing variable angle tow composites," *Composites Part A: Applied Science and Manufacturing*, vol. 43, no. 8, pp. 1347–1356, 2012.
12. R. Kisch, "Automated fibre placement historical perspective," in *Proceedings of the SAMPE '06 international symposium*, (Long Beach, California), pp. 1–65, 2006.
13. B. C. Kim, K. Hazra, P. Weaver, and K. Potter, "Limitations of fibre placement techniques for variable angle tow composites and their process-induced defects," in *18th International Conferences on Composite Materials*, (Jeju, Korea), pp. 1–6, 2011.
14. X. Li, S. R. Hallett, and M. R. Wisnom, "Modelling the effect of gaps and overlaps in automated fibre placement (AFP)-manufactured laminates," *Science and Engineering of Composite Materials*, vol. 22, no. 2, pp. 115–129, 2015.
15. B. C. Kim, P. M. Weaver, and K. Potter, "Manufacturing characteristics of the continuous tow shearing method for manufacturing of variable angle tow composites," *Composites Part A: Applied Science and Manufacturing*, vol. 61, pp. 141–151, 2014.
16. R. L. Lincoln, P. M. Weaver, A. Pirrera, and R. M. J. Groh, "Imperfection-Insensitive Continuous Tow-Sheared Cylinders," *Composite Structures*, vol. 260, no. March, p. 113445, 2021.
17. R. L. Lincoln, P. M. Weaver, A. Pirrera, and R. M. J. Groh, "Optimization of imperfection-insensitive continuous tow sheared rocket launch structures," in *AIAA Scitech 2021 Forum*, no. January, (Virtual), pp. 1–19, 2021.
18. R. L. Lincoln, P. M. Weaver, A. Pirrera, and R. M. J. Groh, "Manufacture and buckling test of a variable-stiffness, variable-thickness composite cylinder under axial compression," in *AIAA SciTech 2022 Forum*, (San Diego, CA), pp. 1–23, 2022.
19. R. M. J. Groh and P. M. Weaver, "Mass Optimisation of Variable Angle Tow, Variable Thickness Panels with Static Failure and Buckling Constraints," in *56th AIAA/ASCE/AHS/ASC Structures, Structural Dynamics, and Materials Conference*, no. January, (Kissimmee, Florida), pp. 1–21, 2015.
20. S. C. White, P. M. Weaver, and K. C. Wu, "Post-buckling analyses of variable-stiffness composite cylinders in axial compression," *Composite Structures*, vol. 123, pp. 190–203, 2015.
21. Z. Wu, P. M. Weaver, and G. Raju, "Postbuckling optimisation of variable angle tow composite plates," *Composite Structures*, vol. 103, pp. 34–42, 2013.
22. A. G. Passos, M. A. Luersen, and C. A. Steeves, "Optimal curved fibre orientations of a composite panel with cutout for improved buckling load using the Efficient Global Optimization algorithm," *Engineering Optimization*, vol. 49, no. 8, pp. 1354–1372, 2017.
23. B. H. Coburn and P. M. Weaver, "Buckling analysis, design and optimisation of variable-stiffness sandwich panels," *International Journal of Solids and Structures*, vol. 96, pp. 217–228, 2016.
24. M. Rouhi, H. Ghayoor, S. V. Hoa, and M. Hojjati, "Multi-objective design optimization of variable stiffness composite cylinders," *Composites Part B: Engineering*, vol. 69, pp. 249–255, 2015.
25. H. Pan, W. Qu, D. Yang, Q. Huang, J. Li, and Y. Ke, "Design and Optimization of Variable Stiffness Composite Cylinders With the Consideration of Manufacturing Interaction," *Applied Composite Materials*, vol. 29, no. 3, pp. 1249–1273, 2022.
26. S. F. Pitton, S. Ricci, and C. Bisagni, "Buckling optimization of variable stiffness cylindrical shells through artificial intelligence techniques," *Composite Structures*, vol. 230, no. May, p. 111513, 2019.
27. J. H. S. Almeida, L. Bittrich, E. Jansen, V. Tita, and A. Spickenheuer, "Buckling optimization of composite cylinders for axial compression: A design methodology considering a variable-axial fiber layout," *Composite Structures*, vol. 222, no. May, p. 110928, 2019.
28. A. W. Blom, C. S. Lopes, P. J. Kromwijk, Z. Gürdal, and P. P. Camanho, "A theoretical model to study the influence of tow-drop areas on the stiffness and strength of variable-stiffness laminates," *Journal of Composite Materials*, vol. 43, no. 5, pp. 403–425, 2009.

29. E. Lindgaard, E. Lund, and K. Rasmussen, "Nonlinear buckling optimization of composite structures considering "worst" shape imperfections," *International Journal of Solids and Structures*, vol. 47, no. 22-23, pp. 3186–3202, 2010.
30. B. Kriegesmann, R. Rolfes, C. Hühne, J. Teßmer, and J. Arbocz, "Probabilistic design of axially compressed composite cylinders with geometric and loading imperfections," *International Journal of Structural Stability and Dynamics*, vol. 10, no. 4, pp. 623–644, 2010.
31. M. W. Hilburger, M. P. Nemeth, and J. H. Starnes, "Shell buckling design criteria based on manufacturing imperfection signatures," *AIAA Journal*, vol. 44, no. 3, pp. 654–663, 2006.
32. V. V. Bolotin, "Statistical Methods in the Nonlinear Theory of Elastic Shells," *Akademii Nauk SSSR, Otdelenie Tekhnicheskykh Nauk [in Russian; English Translation: NASA TTF-85 1962; 1–16].*, vol. 3, pp. 33–41, 1958.
33. J. Arbocz and H. Abramovich, "The initial imperfection data bank at the Delft University of Technology: Part I," tech. rep., Delft University of Technology, Delft, Netherlands, 1979.
34. I. Elishakoff, S. Van Manent, P. G. Vermeulen, and J. Arbocz, "First-order second-moment analysis of the buckling of shells with random imperfections," *AIAA Journal*, vol. 25, no. 8, pp. 1113–1117, 1987.
35. H. Wagner, C. Hühne, and I. Elishakoff, "Probabilistic and deterministic lower-bound design benchmarks for cylindrical shells under axial compression," *Thin-Walled Structures*, vol. 146, p. 106451, 1 2020.
36. C. Schillo, B. Kriegesmann, and D. Krause, "Reliability based calibration of safety factors for unstiffened cylindrical composite shells," *Composite Structures*, vol. 168, no. May, pp. 798–812, 2017.
37. B. Kriegesmann, R. Rolfes, C. Hühne, and A. Kling, "Fast probabilistic design procedure for axially compressed composite cylinders," *Composite Structures*, vol. 93, no. 12, pp. 3140–3149, 2011.
38. Z. Gürdal and R. Olmedo, "In-plane response of laminates with spatially varying fiber orientations - Variable stiffness concept," *AIAA Journal*, vol. 31, no. 4, pp. 751–758, 1993.
39. I. Elishakoff and E. Archaud, "Modified Monte Carlo method for buckling analysis of nonlinear imperfect structures," *Archive of Applied Mechanics*, vol. 83, no. 9, pp. 1327–1339, 2013.
40. C. Runge, "Über empirische Funktionen und die Interpolation zwischen äquidistanten Ordinaten," *Zeitschrift für Mathematik und Physik*, vol. 46, pp. 224–243, 1901.
41. J. F. Epperson, "On the Runge Example," *The American Mathematical Monthly*, vol. 94, no. 4, pp. 329–341, 1987.
42. D. P. Vlasveld, H. E. Bersee, and S. J. Picken, "Nanocomposite matrix for increased fibre composite strength," *Polymer*, vol. 46, pp. 10269–10278, 11 2005.
43. B. Kriegesmann, *Probabilistic design of thin-walled fiber composite structures*. PhD thesis, Gottfried Wilhelm Leibniz University Hannover, 2012.
44. NASA, "Buckling of thin-walled circular cylinders - SP-8007 Revision 2," tech. rep., Langley Research Center, Hampton, VA, 2020.
45. S. Setoodeh, M. M. Abdalla, S. T. IJsselmuiden, and Z. Gürdal, "Design of variable-stiffness composite panels for maximum buckling load," *Composite Structures*, vol. 87, no. 1, pp. 109–117, 2009.
46. S. T. Ijsselmuiden, *Optimal design of variable stiffness composite structures using lamination parameters*. PhD thesis, Delft University of Technology, 2011.
47. J. Grenestedt and P. Gudmundson, "Layup Optimization of Composite Material Structures," in *Optimal Design with Advanced Materials* (P. Pedersen, ed.), no. December, pp. 311–336, 1993.
48. J. L. Akian, "A proof of the convexity of a set of lamination parameters," *Mathematical Methods in the Applied Sciences*, vol. 45, no. 3, pp. 1299–1309, 2022.
49. M. Picchi Scardaoni and M. Montemurro, "Convex or non-convex? On the nature of the feasible domain of laminates," *European Journal of Mechanics, A/Solids*, vol. 85, no. August 2020, p. 104112, 2021.
50. S. C. White and P. M. Weaver, "Towards imperfection insensitive buckling response of shell structures-shells with plate-like post-buckled responses," *The Aeronautical Journal*, vol. 120, pp. 233–253, 2 2016.
51. Dassult Systèmes, "Abaqus 2018," 2018.
52. C. J. McInnes, R. L. Lincoln, A. Pirrera, B. C. Kim, and R. M. J. Groh, "On the Finite Element

Discretization of Continuous Tow-Sheared Structures," in *AIAA SciTech 2022 Forum*, (San Diego, CA), pp. 1–19, 2022.
53. H. Wagner, E. Sosa, T. Ludwig, J. Croll, and C. Hühne, "Robust design of imperfection sensitive thin-walled shells under axial compression, bending or external pressure," *International Journal of Mechanical Sciences*, vol. 156, pp. 205–220, 6 2019.
54. K. Marlett, Y. Ng, and J. Tomblin, "Hexcel 8552 IM7 Unidirectional Prepreg Qualification Material Property Data Report," tech. rep., National Institute for Aviation Research, Wichita, Kansas, 2011.
55. "Python Software Foundation," 2018.
56. J. Onoda, "Optimal laminate configurations of cylindrical shells for axial buckling," *AIAA Journal*, vol. 23, no. 7, pp. 1093–1098, 1985.
57. P. M. Weaver, J. R. Driesen, and P. Roberts, "The effect of flexural/twist anisotropy on compression buckling of quasi-isotropic laminated cylindrical shells," *Composite Structures*, vol. 55, no. 2, pp. 195–204, 2002.
58. C. Hühne, "Robuster Entwurf beulengefährdeter, unversteifter Kreiszylinderschalen aus Faserverbundwerkstoff," *DLR Deutsches Zentrum fur Luft- und Raumfahrt e.V. - Forschungsberichte*, no. 17, pp. 1–211, 2006.
59. Q. Guo, J. Hang, S. Wang, W. Hui, and Z. Xie, "Buckling optimization of variable stiffness composite cylinders by using multi-fidelity surrogate models," *Thin-Walled Structures*, vol. 156, no. May, p. 107014, 2020.